Advanced "Digital Twin" platform for powder-bed fusion additive manufacturing

Jakub Mikula *
Robert Laskowski *
Ling Dai *
Wenjun Ding *
Ming Wei *
Kewu Bai *
Kun Wang *
Ramanarayan Hariharaputran *
Rajeev Ahuwalia *
Guglielmo Vastola *
Yong-Wei Zhang *

* A*STAR Institute of High Performance Computing, 1 Fusionopo + lis Way, #16-16, Singapore 138632.

Powder-bed fusion (PBF) additive manufacturing is a complex process involving powder melting, rapid solidification, pore formation, microstructure evolution, residual stresses, and distortion. Because of this complexity, developing the process for producing a new alloy, or a new powder shape or size distribution, is a complex and expensive task, requiring a series of trial-and-error experiments. This challenge is further exacerbated by the tight coupling between the process and part shape, resulting in process parameters that are acceptable for one design, but not for another. To address this grand challenge, we develop a truly integrated, multiscale simulation platform for the PBF process. By linking modeling capabilities at the part scale and the powder scale, the platform is able to address a multitude of aspects of process development. By exploring the parameter space digitally rather than experimentally, development is faster and cheaper than relying purely on experiments.

● **Key Words :** Additive manufacturing, Multiscale modeling, Powder melting, Microstructure prediction, Mechanical properties, Residual stress, Distortion, INCONEL718　　● **R&D Stage :** Product alpha version

1. Introduction

Following continuous improvements in laser quality and process stability over the last decade, laser powder-bed fusion (L-PBF) additive manufacturing (AM) has experienced tremendous growth and insertion into industrial production. This trend continues to be robust, confirmed by another double-digit growth in 2019, that has put the market size at 11.8 billion US dollars [1]. In production, AM is economically attractive mainly because a) it allows monolithic manufacturing of single parts, and b) it allows the production of part designs that were previously impossible to manufacture by other methods. In case a), after the well-known success of the GE fuel nozzle [2], the industry has seen numerous new applications where PBF simplified the manufacturing process, such as a recent case where the number of components in an impeller was reduced from 73 to 1, which also reduced its weight by 50% [3]. In case b), freedom of design enables new business opportunities by developing new products, such as conformal high-performance heat exchangers, which are simply impossible to manufacture without AM [4]. Taken together, these examples clearly show that AM offers new avenues of business growth, and therefore it is beneficial to invest into this sector.

2. Motivation

In L-PBF, thin layers of powder (layer thickness around 40 μm) are spread in a chamber with a controlled atmosphere, and are exposed to a laser beam. Following the specific scan vectors of the laser, the powder is consolidated into solid metal, ultimately forming the component. As a result, the process is extremely complex, and involves high-energy light-matter interactions, rapid melting and solidification, non-equilibrium microstructure evolution, and the introduction of residual stress. Because of this complexity, not surprisingly, the development process for a new alloy composition, and a new powder batch, usually proceeds by trial-and-error. In this approach, several combinations of laser power, scan speed, and hatch spacing are attempted, until

satisfactory values are found. Because this approach requires many samples, it is material and labor intensive, time consuming, and therefore expensive.

An alternative to the trial-and-error approach is the use of advanced modeling and simulation of the L-PBF process. By performing the tests digitally rather than experimentally, a company can explore process parameters quickly, and at a low cost. Therefore, computer modeling is economically attractive for L-PBF. At the same time, its extraordinary complexity requires deep scientific knowledge and understanding of the process. Further, development of an actual software product requires extensive capabilities in scientific computing, high-performance parallel computations, and software development. Clearly, finding such a wide range of scientific and computational capabilities is not an easy task.

In Singapore, Hitachi partnered with the A*STAR Institute of High Performance Computing (IHPC) to achieve this goal. Because of decades of experience in materials science, photonics, engineering mechanics, and high-performance computing, the collaboration was able to produce an advanced simulation platform for additive manufacturing, the "Digital Twin", which is poised to address a wide variety of manufacturing challenges in L-PBF. In the following, we will proceed to describe the platform step by step, using an impeller component provided by Hitachi as an example. The material used is Hitachi INCONEL 718.

3. Platform architecture

At its foundation, the simulation platform is composed of two main components, namely, the server and the client. The two components are connected to each other through TCP/IP. The server component is where all numerical calculations are performed. It is intended to be compiled on a server-class computer, and is scalable from workstations to supercomputers. In fact, the server takes full advantage of the message-passing interface (MPI) communication protocol to handle heavy workloads in parallel. While performing the calculations, the server also remains responsive because of the built-in asynchronous multithreading. This implementation has the further advantage of allowing multiple clients to connect to the same server. Because of its focus

on numerical calculations, the server is compiled with processor-dependent flags in order to achieve maximum performance, and is tuned for Linux operating systems. Intentionally, the server does not have a graphical user interface (GUI) and is accessible only through TCP/IP.

The user interacts with the client component, which is designed to be lightweight, portable, and focused on the GUI. For example, the client can be installed on both Windows and Linux computers and can run on a laptop. This architecture allows the server and the client to be run in different geographical locations, as well as on cloud infrastructures. The client is built on the Qt5 framework and its rendering is entirely developed using the VTK library.

In the following, we will illustrate the details of the architecture by walking the reader from the beginning to the end of the workflow.

4. Workflow demonstration for selective laser melting of Hitachi IN718 powder

4.1 Component loading and preparation for calculations

The overall platform workflow is schematically demonstrated in **Fig. 1**. User workflow begins by connecting the client to the server through TCP/IP. After the connection is successfully established, the user proceeds by selecting the material model, the printer model, and the process parameters. The choice of process parameters is completely open to the user, and begins with the default values used by the EOS M290 printer.

Next, the component and the support structures are loaded. These are in the form of *.stl files, for example, as produced by preprocessing software such as Materialise Magics [5]. The *.stl files are rendered in the first window of the GUI, as shown in **Fig. 2**.
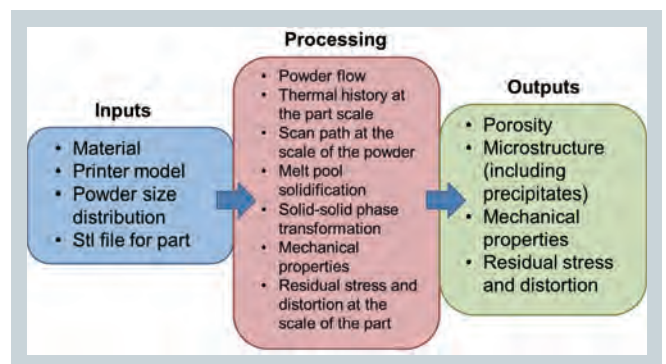

Fig. 1   Overall workflow demonstrating the platform's capabilities

In the next step, the user proceeds by voxelizing the *.stl* file domain to generate a finite element mesh, which is used for thermal and mechanical calculations at the part scale. Here, it is important to note that the mesh is generated on the server side, processed, and then sent to be displayed on the client side.

The user then proceeds to compute the scan pattern. The scan pattern is the actual sequence of laser positions to expose the whole component. Here, the laser exposure is resolved at the scale of each individual stripe, but not descending to the level of the melt pool. This choice is intentional, and aims to reduce the computational cost at the part scale, while retaining a sufficient degree of simulation resolution within each layer. The scan pattern is rendered with red lines representing the midpoint of each stripe, as shown in **Fig. 3**.

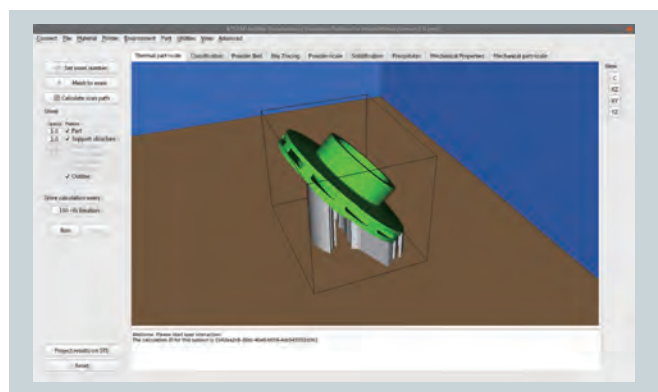The simulation is then started by clicking the 'run' button.

Fig. 2 Component (in green) shown in the graphical user interface, together with the support structures (in grey). The build platform is shown in brown
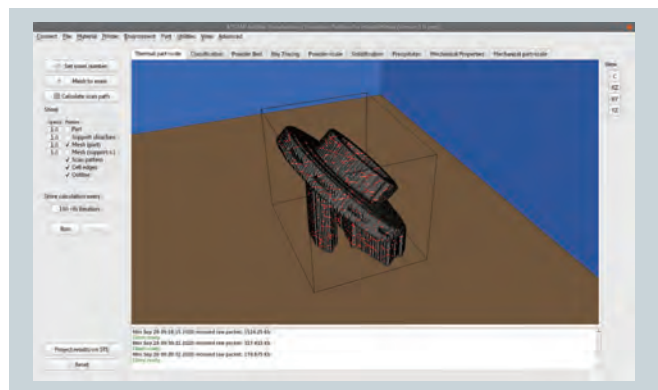

Fig. 3 Scan pattern (red lines) rendered on finite element mesh

4.2 Thermal calculation at part scale

The temperature field T and thermal history $T(t)$ at the scale of the component are computed using the thermal solver that is implemented as a finite element (FE)

discretization of the heat equation accounting for heat conduction and convection:

$$\rho c_p \frac{\partial T}{\partial t} = \nabla \cdot (k \nabla T) + Q - h_\Gamma (T - T_\infty)$$

Eq-4.2.1

This equation is solved on the domain of a voxelized *.stl* file such as shown in **Fig. 3**. Here, ρ is the material density, c_p is the specific heat, k is the thermal conductivity, Q represents the internal heat source, h_Γ is the convection coefficient, and T_∞ represents the ambient temperature. In this report, the material properties of general IN718 are used. The internal heat source Q is described using an ellipsoidal Gaussian distribution that resolves the scan path on the scale of a single stripe. The heat source at each layer moves along the stripes that are shown as red lines in **Fig. 3**. The finite element mesh is assembled in a layer-by-layer fashion, where the number of finite element layers N^{FE} does not necessarily equal the number of real layers N. In fact, the ratio for the case of the voxelized impeller in **Fig. 3** is $N/N^{FE} \approx 10$. This approximation is a necessary step in order to keep the computational cost feasible. However, it is assured in the simulation that the total energy used to build the component is the same irrespective of the number of FE layers. As the total heat Q can be described by the equation $Q = Pt$, any of the parameters (laser power P, printing time t, scan speed v) can be scaled with N/N^{FE} to satisfy this condition.

The finite element discretization of the heat equation results in a transient problem described by a system of linear differential equations that are temporally integrated using the implicit Euler scheme, ensuring the convergence of the solver even for large time steps. An iterative solver is employed using the package Trilinos | Belos [6] to solve the linear system of equations that results from the integration scheme. Iterative solvers are usually faster and more memory efficient when dealing with large systems.

The voxelized domain consists of both the component and the support structure. The support structure is modelled as a solid continuum with rescaled material properties k, c_p, and ρ that homogenize its complex lattice-like structure. Note that a solid *.stl* file for the support structure is required, as seen in **Fig. 2**, as the

fine details of the otherwise lattice-like structure cannot be currently resolved by the voxelization algorithm.

The computed temperature $T(t)$ is stored at each time instance for each node of the FE mesh and can be plotted for each individual node at the end of the simulation (see **Fig. 4**), allowing the user to perform a more detailed analysis of the temperature profiles at various locations. The complete thermal histories (temperature profiles for all nodes) are stored in a *.vtk* file that is later used for classification purposes in which the component is divided into regions that share a similar thermal history.
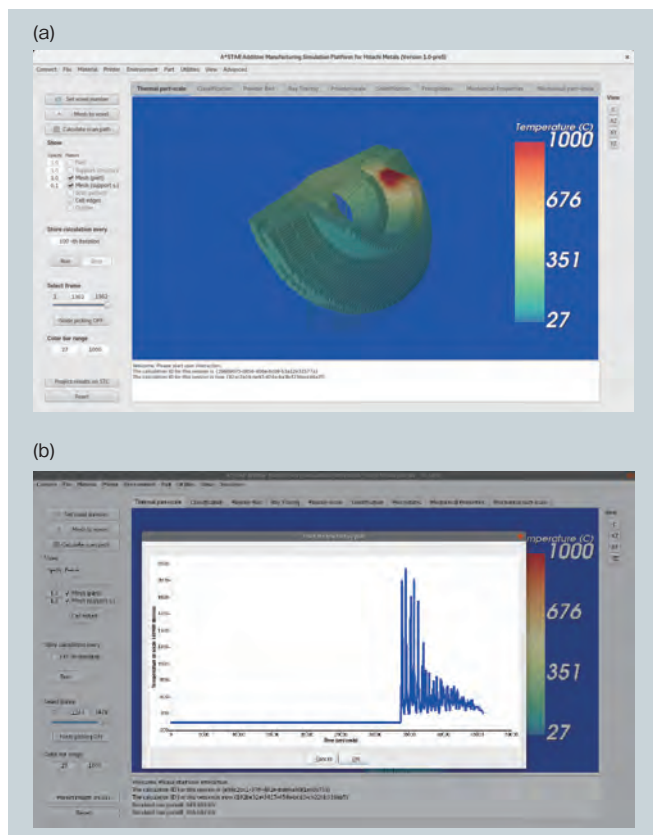

Fig. 4 (a) Snapshot of thermal calculation results at part scale, midway during the build. In this simulation, the scan pattern is resolved at the scale of the individual scan stripe. (b) After the calculation is complete, the user can click on each mesh node, and the corresponding thermal history is plotted in a new window. The temperature spikes resulting from the multiple scan passes are clearly visible.

4.3 Classification of thermal histories

It is expected that the as-printed component will exhibit variations in grain microstructure, mechanical properties and residual stress affected predominantly by geometrical features (thin walls vs. bulk), the scan path, printing process parameters, and cooling rate. While in an ideal scenario these properties would be predicted at each node of the finite element mesh using a much more detailed powder-scale

model, such a simulation approach would be computationally excessively high if not impossible. Therefore, a multi-scale approach is implemented in which the component is divided into a smaller number of regions (classes) that share a similar thermal history and can be treated with a single powder-scale simulation. The properties of reference elements are then interpolated through the entire component domain using a weighted distance algorithm.

While previously, such an approach would require the user to intervene and manually pick the reference elements based on engineering judgement, the component is now classified automatically based on the complete thermal history that was pre-calculated from the thermal solver in the previous step (see **Fig. 3**). The classification is currently done by accounting for the time during which each point remains above a certain temperature, thus also taking into consideration the cooling rate. The number of classes is user-defined. For the purpose of this demonstration, the impeller is divided into 10 classes and the results for the impeller are shown in **Fig. 5**, in which the expected symmetrical shape can clearly be seen.

After the classification is finished, each enclosed domain is attributed a single reference finite element with a characteristic temperature that is passed to the lower powder-scale simulation for a detailed analysis of the printing process resolving the individual grains.
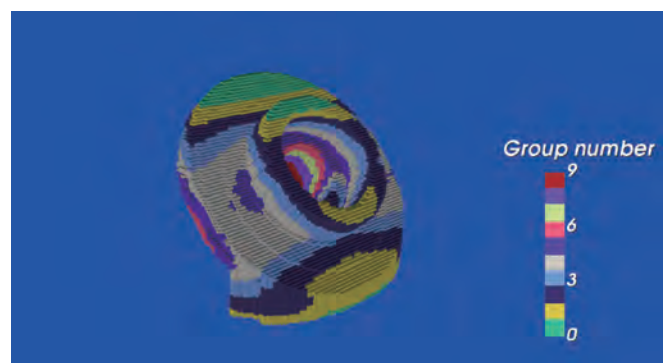

Fig. 5 Classification results illustrating regions with similar thermal histories. In this example, ten groups were chosen. The material in each group is expected to exhibit a similar grain microstructure and mechanical properties.

4.4 Powder-bed calculation

The powder-bed simulation process was coded by means of the discrete element method (DEM)[7]. In this approach, the powder particles are generated from spheres to represent three shapes: spheres, satellites (dual spheres), and ellipsoids. The dynamics of the powder follows

Newton's laws.

All forces, except the gravitational force, arise from collisions among the powder particles or from collisions between the particles and the walls/plates/blades. These forces are computed by overlapping induced Hertz equations [8), 9)].

As shown in **Fig. 6**, the powder particles are generated at certain regions within the simulation cell (**chart-a**), and freely fall onto the loading plate. Once the powder forms a stably piled heap, the loading plate is lifted up, after which a blade slides from the side (**chart-b**). Being pushed by the blade, the powder falls down to the working plate and forms a packed layer (**chart-c**). The excessive powder is scraped aside to the trash well (**chart-d**).
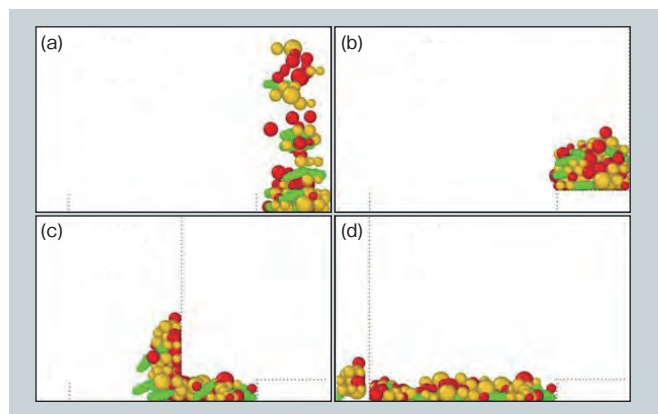

Fig. 6　Discrete element method (DEM) simulation of powder pouring and spreading into a powder bead. The powder is composed of particles with three shapes: spheres (red), satellites of dual spheres (yellow), and ellipsoids (green).

4.5　Ray-tracing calculations

The metal material is represented by an arbitrary surface, which consists of many finite sized rectangular plane surfaces, i.e., meshes. The laser beam is represented by a bundle of rays, with same size (width), wavelength, and each ray having a starting point, incident direction, energy, wavelength and polarization. The size (width) of the rays should be small enough to resolve the surfaces, which requires the number of rays to be large.

Intersection tests are performed for each ray with all surfaces (meshes). If an intersection occurs, the absorption and reflection, including the absorptivity, propagation direction, and remaining energy for each ray, are calculated between the ray and the geometry, taking into account the incidence angle, polarization for each incidence angle, and the optical parameters of the material. After reflection, the ray is updated

with a new energy, starting point, and direction. If no intersection happens for the ray, it propagates out of the simulation space, and is deleted from the simulation. The intersection tests for all rays are repeated until all of them propagate out the simulation space, or their energies are below a threshold value and therefore can be ignored. The ray-mesh (surface) intersections can be treated as line–plane intersections, based on geometric optics and the Fresnel equations.

One point to be noted is that, although the polarization of the laser (direction of the laser electric field) is fixed for each incidence event, the polarization of a ray for each event is different since it is determined by the relation between the incidence plane and the laser polarization. The component of the laser electric field in the incidence plane is the p-polarized part, while the component perpendicular to the incidence plane is the s-polarized part. Both components need to be calculated for every reflection to compute the absorbed energy, as the absorptivity for the two components is different.

The implementation starts with reading geometry parameters (three vertices for each finite rectangular plane (mesh), which have an arbitrary geometrical shape), laser parameters (position of the spot center, spot size, wavelength, and energy) and material parameters (refractive index). The code next creates finite-sized rectangular planes, i.e., meshes, to represent the geometry, and then creates rays for the laser source. It performs intersection tests for each ray with all geometries. If there is an intersection, reflection and absorption are calculated, and the data for each ray are updated, including absorptivity, direction and position of rays. If there is no intersection, the ray is deleted from the simulation. The intersection tests are repeated for all rays, until all rays are either deleted or their energy is absorbed such that the remaining energy falls below a threshold and can therefore be ignored. The energy distribution is calculated for all reflection points, and output for data processing, after which the code ends.

The method is validated by comparing with theory, numerical studies and experiments, for laser interaction with a flat surface and a powder bed. The parameters for the powder are taken from previous literature on experimental characterization or numerical studies. The powder size

distribution is tuned to approach the experimental conditions, so that the validation is more realistic.

For the simplest case, a laser beam incident on a flat surface, our simulation results agree with theory exactly, as shown in **Table 1**. Three materials are modelled: stainless steel, titanium and aluminum. Simulation results published by Lawrence Livermore National Laboratory (LLNL) are also listed for reference [10].

Considering the AM conditions, powder particles with different structures and composed of different materials are tested. A Gaussian distribution of particle size is adopted, as in the experiments at LLNL. The distribution of energy absorbed by the powder is shown in **Fig. 7 (a)**. It can be seen that the distribution is complex and non-

uniform, and depends on the geometry and material. Thus, the ray-tracing method was very effective for determining the absorption distribution, which would be very difficult with any other methods.

As seen in **Table 2**, our simulation results are all within the range of experimental measurements [10], and the accuracy is high because we include higher-order reflections as well as an accurate calculation of the Fresnel equation. [11].

Table 1 Absorptivity of laser energy by flat surface composed of different materials

Material (refractive index)	Theory	Our simulation	Simulation by LLNL [10]
SS (3.27 +i 4.48)	34.15%	34.15%	34%
Ti (3.45 +i 4)	38.54%	38.54%	38%
Al (1.244 +i 10)	4.74%	4.74%	4.7%

Table 2 Absorptivity of laser energy by powder particles with Gaussian size distribution

Material (refractive index)	Experiment by LLNL [10]	Our simulation	Simulation by LLNL [10]
SS (3.27 +i 4.48)	63-68%	66.67%	60%
Ti (3.45 +i 4)	67-72%	70.06%	65%

4.6 Powder-scale calculations

The main physical phenomena at the powder scale are laser energy absorption, thermal transport, phase transitions, grain growth and melt pool flow. Physical phenomena such as thermal history, melt pool size, keyhole size, porosity, grain size, and grain orientation, play a very important role in the AM process and determine the product quality [12]. To perform a simulation that captures these phenomena, Digital Twin powder-scale modeling integrates a thermal solver, phase-transition solver, grain solver and fluid-dynamics solver.

Laser energy absorption, thermal diffusion, thermal radiation, solidification/fusion latent heat, and evaporation latent heat are taken into account in the thermal solver [13], as given in **Eq-4.6.1**,
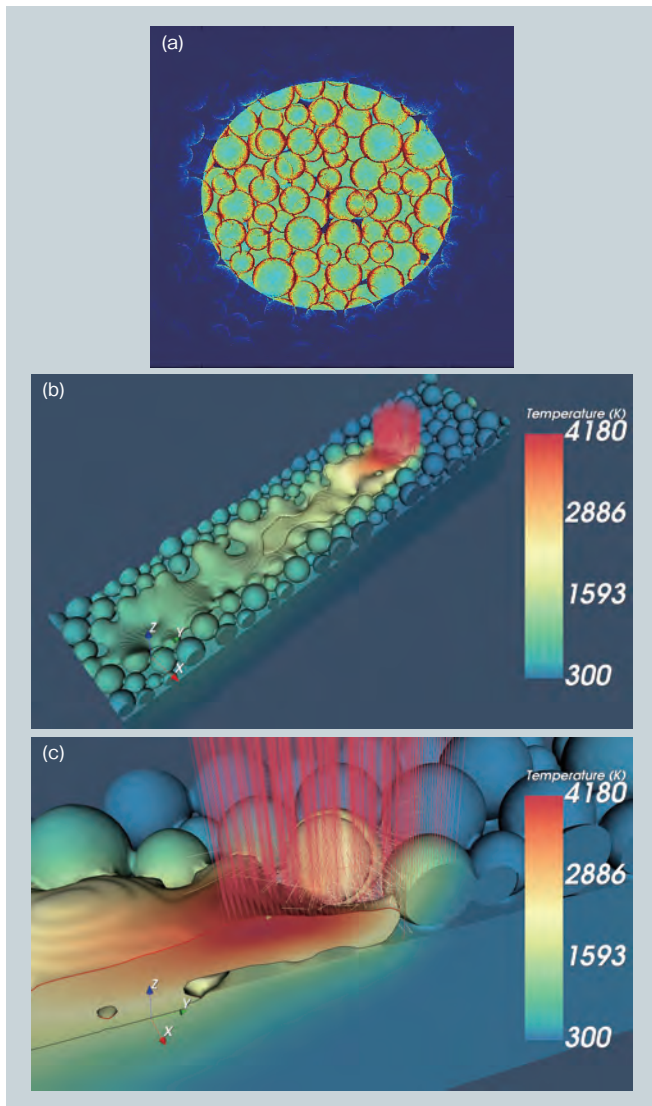

Fig. 7 (a). Energy distribution on powder bed, with Gaussian distribution, irradiated by a laser beam, (b) and (c) On-the-fly ray-tracing calculation for powder-scale simulation. Here, the true energy is calculated, and redistributed into the material as a Gaussian energy source. The primary rays are shown as red lines, while the secondary reflections are shown as yellow segments

$$\rho c_p \left(\frac{\partial T}{\partial t} + T \nabla \vec{u} \right) = \nabla k \nabla T - h \, (T - T_0)$$
$$- \epsilon \sigma \, (T^4 - T_0^4) + q''_{ij,\,laser} - q''_{evap} - d \eta_s \, \Delta H_{ls}$$

Eq-4.6.1

where ρ is the total density, c_p is the heat capacity, u is the flow velocity, k is the thermal conductivity, h is the

convective heat transfer coefficient, ϵ is the emissivity, σ is the Stefan-Boltzmann constant, T_0 is the ambient temperature, q'_{laser} is the laser energy, q''_{evap} is the total evaporation latent heat, η_s is the solid order parameter from the phase field, and ΔH_{ls} is the latent heat of fusion. The terms in **Eq-4.6.1** represent the total heat variation, the heat flux due to liquid/vapor interface flow, diffusion, surface convection, thermal radiation, laser energy, evaporation latent heat and fusion/solidification latent heat. The laser energy may be obtained from the laser ray-tracing module or from the built-in Gaussian and cylindrical models.

A phase-field model is used in the phase-transition and grain solvers [14] with two series of order parameters. The first series describes the phase, e.g. solid η_s, liquid η_l and vapor η_v. The second describes the grains, each initialized with a random orientation. The total free energy F is given in **Eq-4.6.2** - **Eq-4.6.4**.

$$F = \int_V \{ g_{phase} + (\eta^s)^2 \cdot g_{grain} + (1 - \eta^s)^2 \sum_{i=1}^{NG} (\eta^{si})^2 + g_{grad} \},$$

Eq-4.6.2

$$g_{phase} = \rho^2 (\eta^b - 1)^2 \left[(\eta^s - 1)^2 \cdot \Phi(\tau) + (\eta^l - 1)^2 \cdot \Theta(\tau) \right]$$
$$+ (\rho - 1)^2 (\eta^v - 1)^2 + w \sum_{i \neq j} (\eta^i \eta^j)^2,$$

Eq-4.6.3

$$g_{grain} = \frac{1}{4} \sum_{i=1}^{NG} \left[(\eta^{si})^2 - 1 \right]^2 + \frac{3}{4} \sum_{i<j}^{NG} (\eta^{si} \eta^{sj})^2 - \frac{NG-1}{4}$$

Eq-4.6.4

$$g_{grad} = - \sum_{i<j}^{4} k_{ij} \nabla \eta^i \nabla \eta^j - \sum_{i<j}^{NG} k_g \nabla \eta^{si} \nabla \eta^{sj}$$

Eq-4.6.5

where $\tau = T/T_m$, $\Phi(\tau) \rightarrow 1$ when $\tau < 1$, and $\Phi(\tau) \rightarrow 0$ when $\tau > 1$, and $\Theta(\tau) = 1 - \Phi(\tau)$. Here, k is the gradient energy coefficient, w is the potential coefficient, and ρ is the density. The variation of the non-conservative phase and grain order parameters follows **Eq-4.6.6**, while the variation of the conservative density follows **Eq-4.6.7**. M is the temperature dependent mobility.

$$\frac{\partial \eta}{\partial t} = -M \frac{\delta F}{\delta \eta}$$

Eq-4.6.6

$$\frac{\partial \rho}{\partial t} = \nabla M \nabla \frac{\delta F}{\delta \rho}$$

Eq-4.6.7

The lattice-Boltzmann model (LBM) proposed by Fakhari et al. [15] is used in the fluid-dynamics solver. A strategy for projecting the phase field to the viscosity field is applied on the basis of the continuity of the viscosity flux. It has been shown that this model can simulate the interface of binary fluids with moderate density ratios with high accuracy and stability, and can significantly and systematically reduce the parasitic current across the interface. The LBM for simulating the interface h and the LBM for the hydrodynamics g are defined as

$$h_\alpha (\vec{x} + \vec{e}_\alpha \delta t, t + \delta t) = h_\alpha (\vec{x}, t) - \frac{(h_\alpha (\vec{x}, t) - \bar{h}_\alpha^{eq} (\vec{x}, t))}{\tau_\eta + 1/2} + \vec{F}_\alpha^\eta (\vec{x}, t),$$

Eq-4.6.8

$$g_\alpha (\vec{x} + \vec{e}_\alpha \delta t, t + \delta t) = g_\alpha (\vec{x}, t) + \Omega_\alpha (\vec{x}, t) + \vec{F}_\alpha (\vec{x}, t),$$

Eq-4.6.9

where h_α is the phase-field distribution function in the α direction, τ_η is the phase-field relaxation time, and w_α and $\vec{e}_\alpha$ are the weight coefficients and mesoscopic velocity set, respectively. Ω_α is the collision term, and $\vec{F}_\alpha^\eta$ and $\vec{F}_\alpha$ are force terms. More details can be obtained in Ref. [15]

Besides the conventional forces in fluid dynamics, the Marangoni force [16] and the recoil-pressure force [17], which are typical forces occurring during laser processing, are also included in the Digital Twin LBM solver, as shown in **Eq-4.6.10** and **Eq-4.6.11**,

$$F_{Ma} = [(\nabla \eta \cdot \nabla \eta) \cdot \nabla T - (\nabla \eta \cdot \nabla T) \cdot \nabla \eta] \cdot \frac{d\sigma}{dT}$$

Eq-4.6.10

$$F_{rec} = 0.54 \, p_0 \exp \left(\frac{\Delta H_{lv}}{R_v} \cdot \frac{T - T_V}{T} \right) \cdot \nabla_\eta$$

Eq-4.6.11

where σ is the surface tension, p_0 is the ambient pressure, ΔH_{lv} is the evaporation latent heat, R_v is the gas constant.

The inputs for powder-scale simulations consist of material parameters, processing parameters, numerical

parameters, and powder-bed and laser parameters. The initial powder-bed conditions for each layer in the powder-scale simulations are obtained from the powder-bed module, and the laser energy distribution, and the degrees of ray absorption and reflection are obtained from the ray-tracing module. The modules are efficiently coupled inside the Digital Twin platform.

Fig. 8 shows the Digital Twin window and simulation results on the powder scale. After AM, a rough surface containing grains could be observed. The color bar denotes the grain orientation. Because of the integration of the thermal, fluid-dynamics, solid/liquid transition, and microstructure-evolution solvers, the model explicitly resolves the powder, the pores, and the grain microstructure.

Fig. 9 shows a validation of the porosity predictions by comparing with the measured porosity of 27 samples, each produced with a different combination of laser power, scan

speed, and hatch spacing. As can be seen, the porosity predicted by Digital Twin is in good agreement with the measurement results obtained using the Archimedes method [18] and two-dimensional optical microscopy.

The simulation results for the influence of process

Fig. 10 Influence of scan parameters on grain size and shape. (a) microstructure computed for EOS default parameters (laser power 285 W, scan speed 0.96 m/s, hatch spacing 0.11 mm). (b) a smaller grain size, and overall increased grain refinement, is observed using lower energy density parameters, namely a laser power of 218W, a scan speed of 1.2 m/s, and a hatch spacing of 0.14mm.
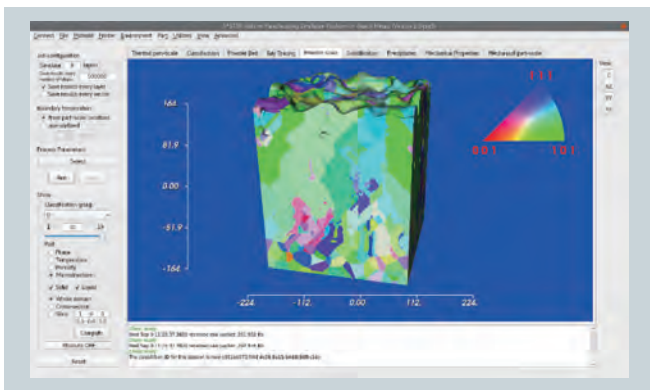

Fig. 8 Digital Twin simulation of laser scan at the powder scale. The integration of thermal, fluid-dynamics, solid/liquid transition, and microstructure evolution solvers allows details concerning the powder, pores, and grain microstructure to be resolved.
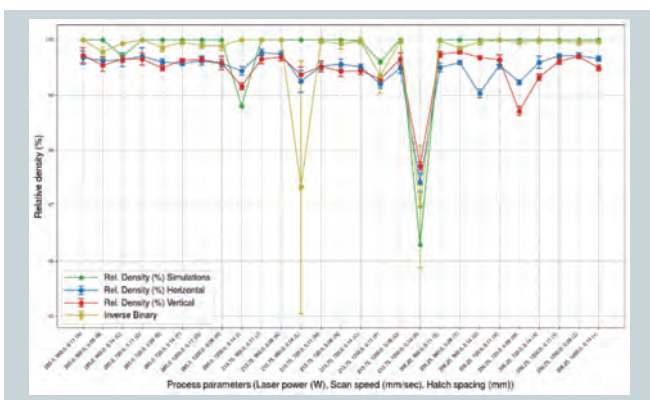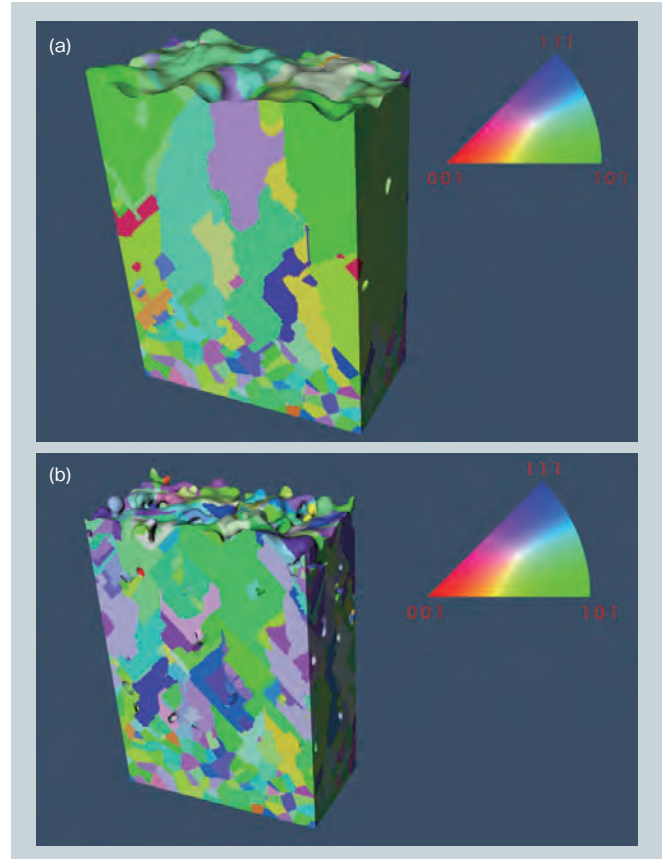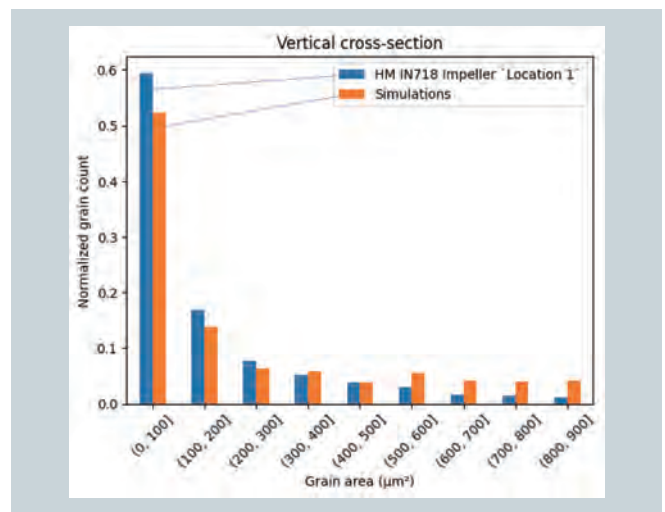

Fig. 9 Validation of porosity predictions by comparison with experimental measurements for 27 samples fabricated with different combinations of laser power, scan speed, and hatch spacing. The blue and red curves show the results of measurements using the Archimedes method. The yellow curve shows the results of measurements using two-dimensional optical microscopy. The green curve shows the simulation results.

Fig. 11 Histogram validation of computed grain size distribution (orange bars) with experimental results for a sample extracted from the impeller component built with Hitachi powder (blue bars).

parameters on grain size and grain shape are shown in **Fig. 10**. A validation histogram for the computed grain size distribution by comparison with experimental results for a sample extracted from an impeller component fabricated using Hitachi powder is shown in **Fig. 11**. The process parameters have an extraordinarily large effect on the grain microstructure, and Digital Twin has the ability to predict and visualize these effects by simulation.

4.7　Solidification at subgrain scale

The microstructure produced during additive manufacturing appears on two different length scales, namely: a) the grain structure with a coarse length scale and b) finer precipitates at a smaller length scale. The columnar grain microstructure is an outcome of the solidification process, and each grain is a collection of cellular structures whose envelope forms the grain boundary. The dynamics of these dendrites is addressed in this section. Since the multicomponent alloy Inconel 718 is computationally complex to simulate, the alloy system is modelled as a pseudo binary alloy with Nb as one component, and with other elements used as the second component.

The microstructural evolution during the solidification process for the IN718 alloy is modeled using the phase-field approach of Wang et $al.$ [19]. In this method, solidification is modelled using the phase order parameter η and the composition variable c. The phase variable takes a value of 1 for the solid phase and -1 for the liquid phase. The composition evolution is simulated using a supersaturation variable U with respect to the far-field composition c_∞

given by $\dfrac{1}{1-k_e}\left(\dfrac{2k_e c\,/\,c_\infty}{1+k_e-(1-k_e)\,\eta}-1\right).$

The evolution equations for the order parameter and the U field are given by

$$\tau_o\,a\,(\hat{n})\Big[\,1-(1-k_e)\,\frac{z-V_p t}{l_T}\,\Big]\frac{d\eta}{dt}$$
$$=\nabla\cdot[\,W(\hat{n})^2\nabla\eta\,]+\eta-\eta^3$$
$$-\lambda g\,(\eta)\Big[\,U+\frac{z-V_p t}{l_T}\,\Big]$$

Eq-4.7.1

and

$$\Big[\,\frac{1+k_e}{2}-\frac{1-k_e}{2}\,\eta\,\Big]\frac{dU}{dt}=\nabla\cdot\Big(Dq\,(\eta)\,\nabla U+$$
$$a\,(\hat{n})\,W\,[\,1+(1-k_e)\,U\,]\,\frac{d\eta}{dt}\,\frac{\nabla\eta}{|\,\nabla\eta\,|}\,\Big)$$
$$-\frac{1}{2}\,[\,1+(1-k_e)\,U\,]\,\frac{d\eta}{dt}$$

Eq-4.7.2

respectively. Besides the material parameters, the evolution is dictated by the temperature gradient and the solidification front velocity, which is determined by the macroscopic process conditions. The model uses a fixed temperature gradient approximation with the gradient imposed only along the z direction. This simulates directional solidification along the z axis which is assumed to be the build direction.

The simulation is initiated with periodic boundary conditions and with an initial alloy composition that becomes supersaturated upon undercooling. The thermal gradients and the solidification velocity are obtained from the powder-scale simulation. As the liquid is undercooled, it results in directional solidification with dendritic cells growing along the thermal gradient direction. Since the transformation happens rapidly, the Nb diffusivity is modelled with finite mobility in the liquid phase and zero mobility in the solid phase. When the liquid is cooled below the liquidus temperature, this negligible diffusivity in the solid results in non-equilibrium composition partitioning at the solid-liquid interface, and hence segregation of Nb occurs at the transformation front. The finite diffusivity in the liquid leads to Nb enrichment in the untransformed liquid. In **Fig. 12**, the simulation was initiated with seeds, a thermal gradient of 10^5 K/m, and a solidification velocity of 4 mm/s. The figure shows the order parameter and the composition for early and late stages of evolution. As can be seen, the dendritic cells grow in size as a function of time. Due the rapid transformation, the inter-dendritic region is enriched with Nb as solidification proceeds, due to the non-equilibrium partitioning. A typical length scale of 0.2 μm is chosen for the computational domain with a characteristic time scale of 4.5×10^{-4} s.

Equations 4.7.1-4.7.2 are solved using an explicit finite difference method. The computations in the simulation are performed using parallel code to speed up the calculations.

The MPI parallel programming library was used for this process. For a given 3D domain, the domain is partitioned in all three directions. The input number of partitions (nx, ny, nz) determines the size of the domain handled by individual processors. The total number of processors needed for the simulation is given by nx × ny × nz.

The solidification tab in the Digital Twin platform hosts this modelling portion, together with the input parameters. The inputs are the temperature gradient and the solidification velocity, which can either be obtained from the powder-scale simulation, or input manually by the user. The composition map is then used as the input for finer-scale microstructure processing and is coupled to the precipitation module.
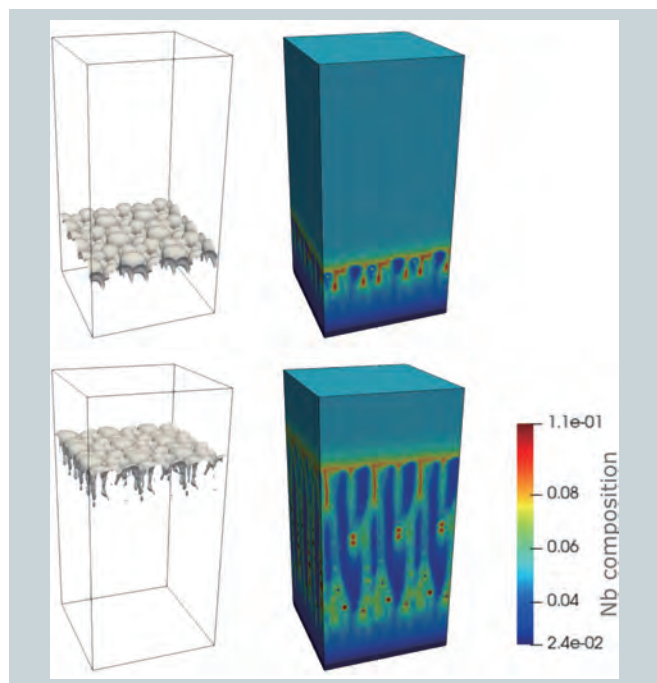

Fig. 12 Three-dimensional simulation of dendritic growth during solidification. The top panel shows the early stage and the bottom panel shows a later stage. The left side shows the surface contours for the dendrites. The right side shows three-dimensional images of the Nb composition estimated using the phase-field model. The Nb enrichment can be observed in the interdendrite regions.

4.8 Simulation of precipitates after solidification

In order to model the mechanical properties of the AM manufactured part, it is also important to incorporate the precipitate phases. The purpose of the solid-state transformation module is to simulate the evolution of precipitate phases in different regions of the as-fabricated part. The typical length scales for precipitate evolution are in the nanometer range. However, the typical sizes of grain and dendritic

regions that are observed during AM are much larger, in the range of several microns. In order to resolve the precipitates, the module adopts the representative volume element (RVE) approach. In order to study precipitate evolution in different regions of the build, RVEs are considered for typical regions of interest, such as bulk regions, grain-boundary regions, dendritic core regions and inter-dendritic regions. These RVEs can have different compositions and thermal histories. The evolution of precipitates for prescribed thermal histories is simulated using the phase-field approach described in detail in the Supplementary Information. To make the model quantitative, we need material properties specific to a given alloy system. The phase-field model is parameterized using the CALPHAD [20] approach based on thermodynamic as well as atomic mobility databases.

As an example, the module has been applied to simulate precipitate evolution in the superalloy IN718. Here we focus on the bulk RVE that represents regions deep inside grains, and so γ'' and γ' are the relevant precipitates (δ precipitates form at grain boundaries). A psuedo ternary Ni-Al-Nb thermodynamic model with surrogate compositions was developed and used to approximate the Gibbs energies for the multi-component IN718 alloy. The atomic mobilities were obtained for a true ternary Ni-Al-Nb alloy from the NIST mobility database [21]. The interfacial energies between the parent and product phases were adopted from reference [22], as were the transformation strains. The elastic constants were taken from reference [23].

The first step is to parameterize the nucleation process. This is achieved by multiple simulations using the model described in the Appendix. Isothermal annealing was simulated for a range of temperatures and for different combinations of nucleation parameters. Fig. 13 (a) shows the simulated time-temperature-transformation (TTT) diagram for the γ'' precipitates. For comparison, the experimental TTT curves taken from references [24] (solid lines), [25] (dashed line) and [26] (dotted line) are also presented. It is clear that our simulated TTT curve is in reasonable agreement with the curve in reference [24]. The precipitate morphologies after 10 h of annealing at 750ºC are shown in Fig. 13 (b). Here, the green precipitates are γ' while the remaining are variants of γ''.

The nucleation parameters used in calculating the TTT

curves in **Fig. 13 (a)** are assumed to be valid for all non-isothermal processes. The model is then used to compute the continuous cooling transformation (CCT) curves and the associated microstructures. To compute the CCT curve, we performed simulations by decreasing the temperature from 1,180ºC to 500ºC at different cooling rates. **Fig. 13 (c)** shows the simulated curve and **Fig. 13 (d)** shows the final morphology for the slowest cooling rate of 0.0041ºC/s. This figure shows that the γ'' precipitates are coarse with plate-like shapes oriented along {100} type planes, while the γ' precipitates are cuboidal.
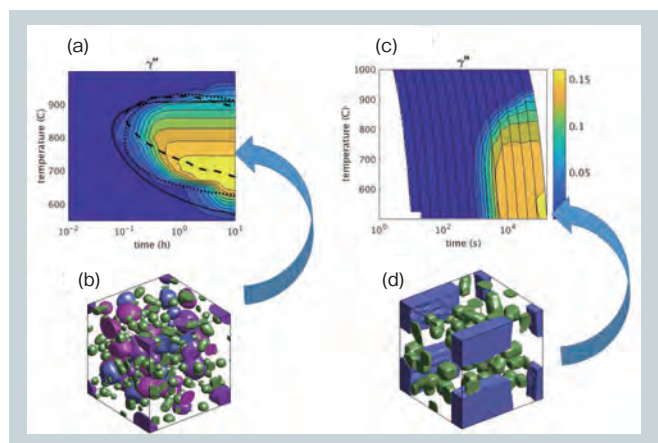

Fig. 13 Calculated TTT diagram for γ'' (a) for the bulk RVE. Experimental TTT curves are displayed for comparison. The solid line in (a) corresponds to the combined $\gamma' + \gamma''$ curve from [23]. The dashed line in (a) corresponds to the combined $\gamma' + \gamma''$ curve from [24]. The dotted line in (a) corresponds to the γ'' curve from [25]. The precipitate microstructure after 10 hours of isothermal annealing at T = 750ºC is shown in (b). Calculated CCT diagrams for γ'' (c) for the bulk RVE. The precipitate microstructure at the end of continuous cooling at a rate of 0.0041ºC/s (d). The microstructures are shown in the basis X $\parallel [100]_\gamma$, Y $\parallel [010]_\gamma$ and Z $\parallel [001]_\gamma$

4.9 Homogenization of mechanical properties

The aim of homogenization is to obtain the constitute law for a single material point that represents a polycrystal such as shown in **Fig. 8**, Here, the self-consistent mean-field approach was employed due to its computational efficiency – the computational time in comparison to the full-field model is reduced from tens of hours to minutes. The self-consistent approximation is a suitable homogenization choice that takes into consideration both the size and shape of the grains. In this approach, each grain is represented by an ellipsoid that best fits the actual shape of the grain through the use of principal component analysis (PCA). The highly elongated grain morphology along the build direction is therefore captured by the large aspect ratio of the principal axis of the ellipsoid.

The homogenization problem for the polycrystal is then simplified into a homogenization problem for ellipsoids embedded in an infinitely large matrix, the properties of which are iteratively searched for. The stress-strain solutions within each inhomogeneity (grain) are obtained through the semi-analytical Eshelby solutions.

The constitutive model for each crystal is described using a rate-independent crystal plasticity model that is largely motivated by reference [27]. This model takes into consideration the effect of the precipitates as well as the Hall-Petch effect that results from the pile-up of dislocations at grain boundaries. The homogenization scheme computes the stress-strain curve for each grain and for the matrix itself. The results for one particular RVE and one loading direction are shown in **Fig. 14**. The bold blue line represents the homogenized stress-strain response of the polycrystal, and the green curves represent the stress-strain response of each grain in the polycrystal. The Young's modulus, yield stress and hardening coefficient are then predicted and passed to the mechanical solver.
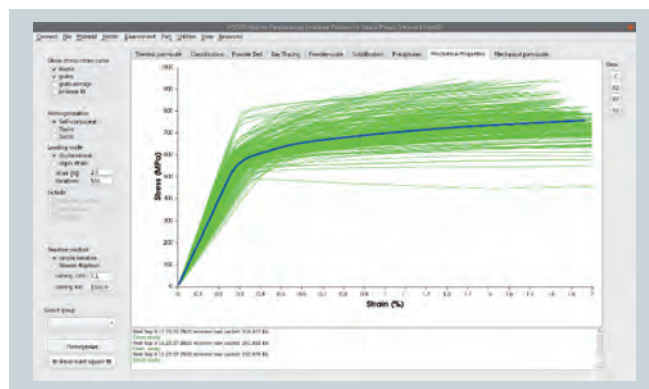

Fig. 14 Statistical crystal plasticity calculation based on the microstructure shown in Fig. 8 Using PCA, the microstructure is post-processed into a set of ellipsoids that best fit the shape and size of each grain. A self-consistent homogenization scheme is then used to calculate the mechanical response of each grain, as well as the homogenized response of the microstructure. The green curves show the response of each grain, the blue curve shows the self-consistent response of the microstructure, and the black curve shows a bi-linear least squares fit.

4.10 Mechanical solver at part scale

Prediction of the residual stresses in 3D printed components is of the utmost importance as they directly correlate with the overall distortion and/or cracking failures. The origin of high stress concentrators may be attributed to geometrical features (such as sharp edges) as well as to the sharp gradients in grain microstructure and mechanical properties across the component.

Mechanical simulations with varying material properties are therefore essential for assessing the effect of both factors in order to find viable solutions and optimize the printing process parameters and the scan-path strategy.

Here, a thermo-mechanical analysis is performed using the simpler inherent-strain finite element approach. The locations of reference elements with the local material properties computed using the lower-level powder-scale simulations are identified from the classification calculations described in Section 4.3. The mechanical properties corresponding to the grain microstructure are predicted from the mean-field self-consistent homogenization model discussed in Section 4.9. These include the Young's modulus E, the Poisson ratio v, the yield stress σ_y, the inherent strain ε^{inh} and the hardening coefficient h. The stress-strain curves obtained using the homogenization model are then least-squares fitted with a bi-linear curve that represents the elasto-plastic behavior at the component scale. The stress σ and strain ε fields are derived from the displacement field u through the simple constitutive law:

$$\sigma = C : \varepsilon^{el} = C : (\varepsilon - \varepsilon^{inh} - \varepsilon^p)$$

Eq-4.10.1

where ε^{el} is the elastic strain, ε is the total strain tensor $\varepsilon_{ij} = 1/2 \ (\partial u_i / \partial x_j + \partial u_j / \partial x_i)$ in which $u = (u_x, u_y, u_z)$ is the displacement field vector and x is the position vector. Here, C is the tensor of elastic constants, the components of which depend on E and v, and ε^p is the plastic strain tensor.

The displacement field u is solved using the same finite element mesh as the one generated for the thermal solver (see **Fig. 3**). The finite element solution is found by minimizing the total strain energy functional W:

$$W = \frac{1}{2} (\varepsilon - \varepsilon^p - \varepsilon^{inh}) : C : (\varepsilon - \varepsilon^p - \varepsilon^{inh})$$

Eq-4.10.2

Minimization of this functional (within the FE framework) leads to a system of linear equations $Ku = F$, where K is the global stiffness matrix and F is the global vector of nodal forces.

The finite element mesh in the simulation is assembled in a layer-by-layer fashion. A snapshot of the simulation is presented in **Fig. 15**, which shows (in **(a)** panel) the displacement field $\underline{u}_y$ component midway through the build and (in **(b)** panel) the overall deformation of the fabricated component at the end of the simulation, where the colors represent the norm of the displacement field

$$| u | = \sqrt{ u_x^2 + u_y^2 + u_z^2 } .$$

The deformation of the component in **Fig. 15** is purposely magnified forty times in order to better visualize the bulging of the impeller edges. It can be seen that the support structure that is shown as transparent is more compliant. Here, the support structure is modeled as a solid continuum (without resolving its complex lattice-like structure) with the material properties, specifically stiffness, scaled down by a user-defined factor.

The computed fields that can be visually outputted and analyzed from this simulation include the displacement (u_i), the stress (σ_{ij}), the total strain (ε_j), and the equivalent plastic strain $\bar{\varepsilon}^p$.
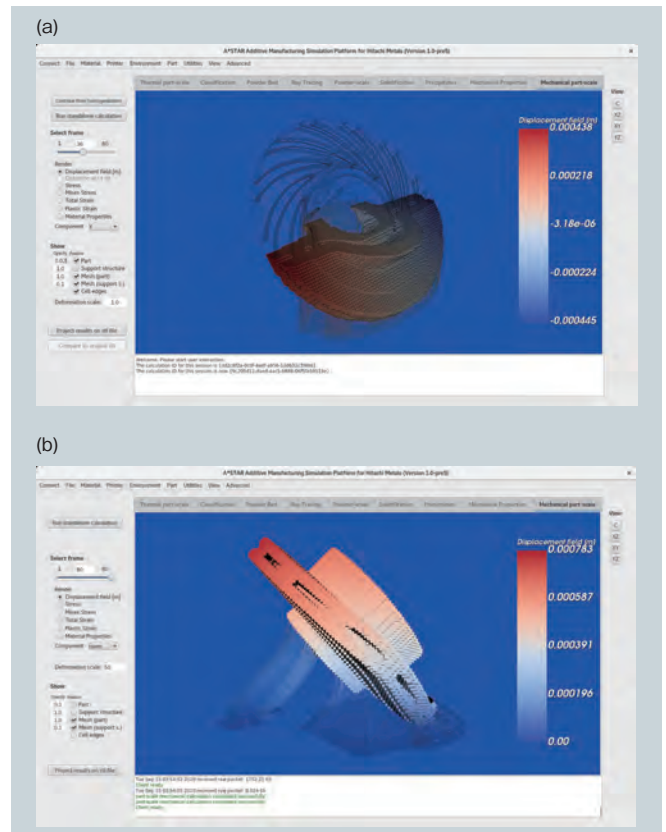

Fig. 15 Mechanical calculation of component distortion and residual stress at part scale. The calculation utilizes the mechanical properties computed by the homogenization scheme, and the intrinsic strain from thermal cooling. (a) displacement field midway through the build, together with the original component and support structures. (b) final distorted shape magnified forty times, showing large deformation of the support structures, as well as forward bending of the impeller sides.

5.　Conclusions

In conclusion, we have developed a truly integrated multiscale simulation platform for powder-bed fusion additive manufacturing which addresses the thermal history at the part scale, classification in key regions, melt-pool dynamics, explicit pore resolution, microstructure, solidification, precipitates, mechanical properties, distortion and residual stresses. Through this integration, the platform is able to address challenges beyond individual length or time scales, such as how the thermal history at the part scale influences the local mechanical properties. As we continue our fruitful collaboration with Hitachi, we are eager to apply the Digital Twin platform to a variety of industrial problems, and support Hitachi's business growth.

6.　Acknowledgments

References

1 ） Terry Wohlers, "Wohlers Report," Wohlers Associates, Fort Collins, CO, USA, 2020.

2 ） D. M. Dietrich, M. Kenworthy and E. A. Cudney, Additive Manufacturing Change Management: Best Practices, CRC Press, 2019.

3 ） Jabil, "DfAM: Redesigning How We Think About Manufacturing, "2020. [Online]. Available: https://www.jabil.com/capabilities/additive-manufacturing/design-for-additive-manufacturing.html. [Accessed October 2020].

4 ） Aerospace Manufacturing, "All change for heat exchange production, "29 September 2020. [Online]. Available: https://www.aero-mag.com/all-change-for-heat-exchange-production/.

5 ） "Materialise Magics Product Information," [Online]. Available: https://www.materialise.com/en/software/magics/product-information.

6 ） M. A. Heroux, R. A. Bartlett, V. E. Howle, R. J. Hoekstra, J. J. Hu, T. G. Kolda, R. B. Lehoucq, K. R. Long, R. P. Pawlowski, E. T. Phipps, A. G. Salinger, H. K. Thornquist, R. S. Tuminaro and e. al, "An overview of the Trilinos project," *ACM Transactions on Mathematical Software*, vol. 31, no. 3, 2005.

7 ） C. Kloss, C. Goniva, A. Hager, S. Amberger and S. Pirker, "Models, algorithms and validation for opensource DEM and CFD–DEM," *Progress in Computational Fluid Dynamics*, vol. 12, no. 2-3, pp. 140-152, 2012.

8 ） A. D. Renzo and F. P. D. Maio, "Comparison of Contact-force Models for the Simulation of Collisions in DEM-based Granular Flow Codes, "*Chem. Eng. Sci.,* vol. 59, pp. 525-541, 2004.

9 ） A. D. Renzo and F. P. D. Maio, "An Improved Integral Non-linear Model for the Contact of Particles in Distinct Element Simulations,"*Chem. Eng. Sci.,* vol. 60, pp. 1303-1312, 2005.

10) C. D. Boley, S. A. Khairallah and A. M. Rubenchik, *App. Opt.,* vol. 54, p. 2477, 2015.

11) A. Rubenchik, S. Wu, S. Mitchell, I. Golosker, M. Leblanc and N. Peterson, *App. Opt.,* vol. 54, p. 7230, 2015.

12) L. Yang, K. Hsu, B. Baughman, D. Godfrey, F. Medina, M. Menon and S. Wiener, Additive Manufacturing of Metals: The Technology, Materials, Design and Production, Springer, 2017.

13) M. Bayat, A. Thanki, S. Mohanty, A. Witvrouw, S. Yang, J. Thorborg, N. Skat Tiedje and J. Henri Hattel, "Keyhole-induced porosities in Laser-based Powder Bed Fusion (L-PBF) of Ti6Al4V: High-fidelity modelling and experimental validation,"*Additive Manufacturing*, vol. 30, p. 100835, 2019.

14) L.-X. Lu, N. Sridhar and Y.-W. Zhang, "Phase field simulation of powder bed-based additive manufacturing," *Acta Materialia*, vol. 144, pp. 801-809, 2018.

15) A. Fakhari, T. Mitchell, C. Leonardi and D. Bolster, "Improved locality of the phase-field lattice-Boltzmann model for immiscible fluids at high density ratios," *Phys. Rev. E*, vol. 96, p. 053301, 2017.

16) D. Höche, S. Müller, G. Rapin, M. Shinn, E. Remdt, M. Gubisch and P. Schaaf, "Marangoni Convection during Free Electron Laser Nitriding of Titanium," *Metallurgical and Materials Transactions B*, vol. 40, p. 497–507, 2009.

17) H. E. Cline and T. R. Anthony, "Heat treating and melting material with a scanning laser or electron beam," *Journal of Applied Physics*, vol. 48, p. 3895, 1977.

18) A. B. Spierings, M. Schneider and R. Eggenberger, "Comparison of Density Measurement Techniques for Additive Manufactured Metallic Parts," *Rapid Prototyping Journal*, vol. 17, pp. 380-386, 2011.

19) T. X. Wang, P. Liu, Y. Ji, Y. Liu, M. Horstemeyer and L. Chen, "Investigation on Microsegregation of IN718 Alloy During Additive Manufacturing via Integrated Phase-Field and Finite-Element Modeling," *J. Mater. Eng. Perform.*, vol. 28, p. 657, 2019.

20) K. Wu, F. Zhang, S. Chen, W. Cao and Y. Chang, "A Modeling Tool for the Precipitation Simulations of Superalloys During Heat Treatments," in *Proceedings of the International Symposium on Superalloys*, 2008.

21) N. m. dataset, NIST, [Online]. Available: https://materialsdata.nist.gov/handle/11256/942.

22) N. Zhou, D. C. Lv, H. Zhang, D. McAllister, F. Zhang, M. J. Mills and Y. Wang, "Computer simulation of phase transformation and plastic deformation in IN718," *Acta Materialia*, vol. 60, pp. 270-286, 2014.

23) "The Materials Project," [Online]. Available: https://materialsproject.org/.

24) R. G. Thomson, J. Dobbs and D. Mayo, "The effect of heat treatment in microfissuring in Alloy 718," *Weld J.*, pp. 299-304, 1986.

25) A. Oradei-Basile and J. F. Radavich, "A current TTT diagram for wrought alloy 718," in *Superalloys 718,625 and various derivatives*, TMS, 1991, pp. 325-335.

26) H. Chandler, Heat Treater's Guide: Practices and Procedures for Nonferrous Alloys, USA: ASM International, 1996.

27) S. Ghorbanpour, M. Zecevic, A. Kumar, M. Jahedi, J. Bicknell, L. Jorgensen, I. Beyerlein and M. Knezevic, "A crystal plasticity model incorporating the effects of precipitates in superalloys: Application to tensile, compressive, and cyclic deformation of Inconel 718," *International Journal of Plasticity*, vol. 99, pp. 162-185, 2017.

28) S. G. Kim, W. T. Kim and T. Suzuki, "Phase field model for binary alloys," *Phys. Rev. B*, vol. 60, pp. 7186-7197, 1999.

29) J. D. Robson, M. J. Jones and P. B. Prangnell, "Acta Materialia," *Extension of the N-model to predict competing homogeneous and heterogeneous nucleation*, vol. 51, pp. 1453-1468, 2003.

30) J. Svodoba, F. Fischer, P. Fratzl and E. Kozechnik, "Modeling of kinetics in multi-component multi-phase systems with spherical precipitates I: Theory," *Materials Science and Engineering A*, vol. 385, pp. 166-174, 2004.

Ming Wei
Institute of High Performance Computing
Agency for Science, Technology and Research (A* STAR)

Kewu Bai
Institute of High Performance Computing
Agency for Science, Technology and Research (A* STAR)
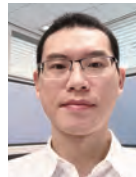
Kun Wang
Institute of High Performance Computing
Agency for Science, Technology and Research (A* STAR)

Ramanarayan Hariharaputran
Institute of High Performance Computing
Agency for Science, Technology and Research (A* STAR)

Rajeev Ahuwalia
Institute of High Performance Computing
Agency for Science, Technology and Research (A* STAR)

Jakub Mikula
Institute of High Performance Computing
Agency for Science, Technology and Research (A* STAR)

Guglielmo Vastola
Institute of High Performance Computing
Agency for Science, Technology and Research (A* STAR)

Robert Laskowski
Institute of High Performance Computing
Agency for Science, Technology and Research (A* STAR)

Yong-Wei Zhang
Institute of High Performance Computing
Agency for Science, Technology and Research (A* STAR)

Ling Dai
Institute of High Performance Computing
Agency for Science, Technology and Research (A* STAR)

Wenjun Ding
Institute of High Performance Computing
Agency for Science, Technology and Research (A* STAR)